Diagenetic Attenuation of Carbon Isotope Excursion Recorded by Planktic Foraminifers during the Paleocene-Eocene Thermal Maximum

Reinhard Kozdon [1], D. Clay Kelly [2], John W. Valley [2, 3]

[1] Lamont-Doherty Earth Observatory of Columbia University, Palisades, New York 10964, USA; [2] Department of Geoscience, University of Wisconsin, Madison, Wisconsin 53706, USA; [3] WiscSIMS, Department of Geoscience, University of Wisconsin, Madison, Wisconsin 53706, USA

Corresponding author: Reinhard Kozdon (rkozdon@ldeo.columbia.edu)

Key Points:

- In situ analysis in planktic foraminifers reveal that the C-isotope excursion (CIE) marking the onset of the PETM is at least 4.6 per mille for surface-ocean DIC
- CIE magnitudes registered by surface-ocean dissolved inorganic carbon and terrestrial substrates are highly congruent at the PETM onset
- the C-isotope composition of diagenetic calcite indicates that many planktic foraminifer records of the CIE are attenuated by diagenesis

Abstract

Earth surface temperatures warmed by ~5ºC during an ancient (~56 Ma) global warming event referred to as the Paleocene-Eocene thermal maximum (PETM). A hallmark of the PETM is a carbon isotope excursion (CIE) signaling the release of massive amounts of ^{13}C-depleted carbon into the ocean-atmosphere system, but substrate-specific differences in the CIE magnitude are a source of uncertainty for estimating the mass of carbon emitted. Here we report that SIMS-based *in situ* measurements of δ^{13}C in minute (7 μm) domains of planktic foraminifer shells (ODP Site 865, central Pacific Ocean) yield a CIE that is ~2‰ larger than that delineated by conventional 'whole-shell' δ^{13}C values for this same PETM record. SIMS-based measurements on diagenetic crystallites yield δ^{13}C values (~2.8‰) that fall between those of pre-CIE and CIE planktic foraminifer shells, indicating that the crystallites are an amalgamated blend of pre-CIE and CIE carbonate. This suggests that diagenesis shifts the whole-shell δ^{13}C compositions of pre-CIE and CIE foraminifers found in samples straddling the base of the PETM interval toward the intermediate δ^{13}C composition of the crystallites thereby dampening the amplitude of the isotopic excursion. The diagenetic process envisioned would be most consequential for carbonate-rich PETM records that have suffered chemical erosion of pre-CIE carbonate. Given that the domains targeted for SIMS analysis may not be pristinely preserved, we consider the 4.6‰ excursion in our SIMS-based δ^{13}C record to be a conservative estimate of the full CIE for surface-ocean dissolved inorganic carbon.

1 Introduction

The Paleocene-Eocene thermal maximum (PETM) was the most prominent in a series of 'thermal maxima' to have punctuated the greenhouse climate state that prevailed over much of the early Paleogene period (e.g., Cramer et al., 2003; Nicolo et al., 2007). This geologically brief (~200 ka) episode of global warming brought a close to the Paleocene epoch at ~56 Ma (Westerhold et al., 2017), and entailed a rapid ~5°C increase in surface temperatures that perturbed the functional partitioning of Earth's biogeochemical systems (e.g., Bowen et al., 2004; Huber and Sloan, 2000; Zachos et al., 2003). The environmental changes wrought by PETM conditions profoundly impacted the global biosphere, altering the complexion of terrestrial and marine ecosystems (e.g., Gingerich, 2006; Thomas, 1990; Wing et al., 2005). Thus, the onset of PETM conditions left an indelible mark on the rock and fossil records, but its most widely recognized signature is a sharp decline in the carbon isotopic (δ^{13}C) compositions of marine and terrestrial materials (Kennett and Stott, 1991; Koch et al., 1992). This negative carbon isotope excursion (CIE) has been documented at numerous locations in various organic and inorganic substrates (e.g., Bowen et al., 2001; Cui et al., 2011; McCarren et al., 2008; Pagani et al., 2006); hence, its ubiquitous nature signals the release of massive quantities of isotopically light carbon into the ocean-atmosphere system (Dickens et al., 1995).

Delineating the CIE in the geologic record provides a chemostratigraphic framework for studying the dynamics of carbon cycling and climate change during the PETM, yet such critical aspects of the CIE as the source(s) of emitted carbon, mass of carbon input, and rate of carbon release are still debated (see Dickens, 2011). Criteria such as the $\delta^{13}C$ composition of the carbon source (Dickens et al., 1995; Higgins and Schrag, 2006), extent of carbonate dissolution in the oceans (Dickens et al., 1997; Zeebe et al., 2009), and degree of climatic warming (e.g., Zeebe et al., 2009) have all been used to assess the veracity of proposed carbon sources and constrain the mass of carbon released into the ocean-atmosphere system during the PETM. The parameter most widely used to constrain the mass of carbon input is the magnitude of the CIE (e.g., Dickens et al., 1995; Gutjahr et al., 2017; Kirtland Turner and Ridgwell, 2016; Pagani et al., 2006; Svensen et al., 2004), but substrate-specific differences in the size of the excursion are a major source of uncertainty for this critical constraint (Bains et al., 2003). Such discrepancies are most evident between terrestrial and marine records that yield mean CIE magnitudes of ~4.7‰ and ~2.8‰ (McInerney and Wing, 2011), respectively. This disparity is puzzling since gas exchange across the air-sea interface is instantaneous on geologic timescales, so the CIE magnitude in marine records expressing the $\delta^{13}C$ of dissolved inorganic carbon in the surface ocean (surface DIC) should be similar to that seen in terrestrial records expressing the $\delta^{13}C$ of atmospheric CO_2 (e.g., Böhm et al., 2002; Koch et al., 1992).

A number of processes and feedback mechanisms have been invoked to reconcile this inter-reservoir discrepancy, while only a handful of studies have given due consideration to the role that seafloor diagenesis may have played in attenuating the CIE recorded by marine carbonates (Bralower et al., 2014; Cohen et al., 2007; Handley et al., 2008; McCarren et al., 2008). This is especially true for CIE records based on the $\delta^{13}C$ of calcite in planktic foraminifer shells. And while the specter of diagenesis has been broached in the literature, its impact on CIE records remains poorly understood and quantitatively unconstrained. This shortcoming is both surprising and understandable. It is surprising from the standpoint that diagenesis is pervasive in seafloor sediments (e.g., Schrag et al., 1995) as evidenced by the paucity of pristinely preserved (glassy) foraminifer shells in the deep-sea sedimentary record (Pearson et al., 2001). On the other hand, it is understandable because the minute, micrometer scales over which this diagenetic alteration occurs within individual foraminifer shells (Sexton et al., 2006) prohibits the use of conventional gas-source mass spectrometry (GSMS) requiring acid digestion of whole foraminifer shells.

Here, we quantify the effects of post-depositional diagenesis on the CIE using new $\delta^{13}C$ data acquired *in situ* by secondary ion mass spectrometry (SIMS) from minute ~7 µm domains within individual planktic foraminifer shells recovered at Ocean Drilling Program (ODP) Site 865. These $\delta^{13}C_{SIMS}$ data indicate that the CIE magnitude recorded by planktic foraminifer shells calcified in the oceanic mixed layer approaches ~5‰, and is therefore more congruous with the CIE magnitude measured from terrestrial materials and organic carbon. In addition, we present complementary $\delta^{13}C_{SIMS}$ data acquired from diagenetic crystallites

that provides sorely needed insight into the mechanistic process by which diagenesis attenuates the magnitude of the CIE registered by planktic foraminifer $\delta^{13}C_{GSMS}$ records.

2 Materials and Methods

2.1 Study site and foraminifer shells selected for *in situ* analysis

Study materials are from two PETM records recovered at Site 865 (hole 865B: 18º26.415'N, 179º33.349'W, 1516.2 m water depth; hole 865C: 18º26.425'N, 179º33.339'W, 1517.4 m water depth), located atop Allison Guyot in the Mid-Pacific Mountains (Sager et al., 1993, Fig. 1A). Benthic foraminifer assemblages indicate that both PETM sections were deposited at mid-bathyal (~1300 m) water depths, and paleolatitude projections place Site 865 near the equator during the late Paleocene (Sager et al., 1993). Previously published $\delta^{13}C$ records (Bralower et al., 1995a) have constrained the PETM to a thin (~15-20 cm) stratigraphic interval in both study sections (Fig. 1B). The two PETM sections are composed of weakly lithified, calcareous ooze from which foraminifer shells were gleaned by rinsing the sediment with pH buffered (~8.0), deionized water over a 63-μm sieve and oven-dried at ~30ºC overnight.

Shells of the planktic foraminifer species *Morozovella velascoensis* and *M. allisonensis* from the hole 865C section were targeted for $\delta^{13}C_{SIMS}$ analysis. Previous studies have shown that the stable isotopic signatures of these two species exhibit size-dependent trends that are similar to those of modern mixed layer-dwelling planktic foraminifers hosting algal symbionts (Kelly et al., 1998; 2001). At Site 865, the $\delta^{13}C$ compositions of *M. velascoensis* and *M. allisonensis* increase by ~0.75 to 1.0‰ over shell sizes ranging between ~150 to 355 μm (Kelly et al., 1998; 2001). To minimize the effects of such $\delta^{13}C$/size variation, geochemical measurements were restricted to a narrow range (300-355 μm) of shell sizes (e.g., Bralower et al., 1995b; Kelly et al., 1996; Kelly et al., 1998). Accordingly, *M. velascoensis* was used for pre-CIE (104.00, 103.70, and 103.50 meters below seafloor, mbsf) and post-CIE (102.00, 101.60, and 101.30 mbsf) samples, whereas the 'excursion taxon' *M. allisonensis* was used for CIE samples (103.00 and 102.90 mbsf). We targeted the hole 865C record for study because a wealth of conventional, whole-shell stable isotope data has been published for both *M. velascoensis* and *M. allisonensis* (300-355 μm size fraction) from this same PETM section (Bralower et al., 1995b; Kelly et al., 1996; Kelly et al., 1998). Added incentive for studying the Site 865 PETM records is provided by an earlier study (Kozdon et al., 2013) that found diagenetic crystallites (~500 μm diameter) composed of translucent crystals of calcite cementing numerous foraminifer shells and fragments in the neighboring hole 865B PETM section (Fig. 2A). Thus, $\delta^{13}C_{SIMS}$ analyses were performed on the diagenetic crystallites for comparative purposes. In short, the CIE recorded by morozovellids from hole 865C was measured by performing 29 $\delta^{13}C_{SIMS}$ analyses in nine shells of pre-CIE *M. velascoensis*, 11 $\delta^{13}C_{SIMS}$ analyses in four shells of the CIE taxon *M. allisonensis*, and 11 $\delta^{13}C_{SIMS}$ analyses in four shells of post-CIE *M. velascoensis.* An additional 35 $\delta^{13}C_{SIMS}$ analyses were performed on 4 diagenetic crystallites recovered from the hole 865B PETM section (Fig. 2A) as well as

four $\delta^{13}C_{SIMS}$ analyses on a smaller crystallite found inside a shell of *M. allisonensis* from the hole 865C (Figs. 2C, D).

2.2 *In situ* carbon isotope analysis by ion microprobe

Foraminifer shells and crystallites were cast with two grains of UWC-3 calcite standard in epoxy and polished to midsection with a relief <1 μm (Kita et al., 2009). To minimize instrumental bias related to sample position, each epoxy mount was prepared such that all analytical pits were within 5 mm of the center of the mount (Kita et al., 2009). After SEM imaging using backscattered electron (BSE) and secondary electron (SE) detectors to identify suitable domains near the base of muricae blades for *in situ* analysis (see Kozdon et al., 2011, 2013), samples were analyzed in two sessions (July and August 2012) by a CAMECA ims-1280 ion microprobe at the WiscSIMS (Wisconsin Secondary Ion Mass Spectrometer) Laboratory (Kita et al., 2009; Valley and Kita, 2009). In both sessions, the $^{133}Cs^+$ primary beam with an intensity of ~600 pA and a total accelerating voltage of 20 keV was focused to a diameter of ~7 μm on the sample surface. Sample charging was compensated by a conductive Au-coat of the sample mounts in combination with an electron flood gun. Tuning of the secondary optics was similar to Kita et al. (2009), and aimed to achieve high secondary ion transmission. Secondary C^- ions were detected simultaneously by a Faraday cup ($^{12}C^-$) and an electron multiplier ($^{13}C^-$). In the second session, $^{13}CH^-$ was included into the analytical protocol and measured simultaneously by a second electron multiplier. Typical $^{12}C^-$ count rates were between ~$5x10^6$ and $6x10^6$ counts per second (cps). The total analytical time per spot was about 5 minutes including pre-sputtering (1 min), automatic centering of the secondary ion image (~1 min), and analysis (20 cycles of 8 seconds each). The gain of the electron multiplier was monitored before the third analysis of each group of four standard analyses (about once every hour), and the applied high voltage was adjusted to compensate drift of the gain of the electron multiplier, if required. Reproducibility of $\delta^{13}C$ of the bracketing standard analyses includes the drift of the gain of the electron multiplier.

Grains of UWC-3 ($\delta^{13}C$ = –0.91‰ VPDB, Kozdon et al., 2009), mounted in the center of each epoxy mount, were measured in four spots before and after <13 sample analyses, and the resulting average value bracketing the samples was used for instrumental mass fractionation (IMF) correction. Reproducibility of the individual spot analyses of UWC-3 standard (bracketing samples) is assigned as uncertainty of unknown samples, and varies from 0.3‰ to 1.4‰ with an average of 0.7‰ (±2 SD, 17 standard-sample-standard brackets were performed in total; see Table S1 in the supporting information). The first standard-sample-standard bracket of the August 2012 session features the highest standard deviation (1.4‰) due to some instability of the primary beam intensity that occurred after instrument startup. A total of 190 analyses were performed, including 100 UWC-3 measurements bracketing the samples. The complete data set and additional details of the methodology can be found in the supporting information (Table S1; see also Craig, 1957; Kita et al., 2009; Kozdon et al., 2009; Kozdon et al., 2011; Valley and Kita, 2009). Whenever

possible, multiple $\delta^{13}C_{SIMS}$ measurements were taken in an individual shell. Replicate $\delta^{13}C_{SIMS}$ analyses within the same chamber are typically within analytical precision.

Several parameters and procedures were used to assess the quality of the data and to identify measurements of domains crosscutting unwanted secondary phases that need to be excluded from the dataset. The secondary ion intensity ($^{12}C^-$ count rate in cps) of the sample analysis was compared to the average $^{12}C^-$ count rate of the eight bracketing standard analyses. Assuming a stable primary beam, only sample measurements with $^{12}C^-$ count rates between 90% and 105% of those of the bracketing standards were used (see Table S1 in the supporting information). Some measurements in crystallite #3 are slightly below the 90% threshold but considered as 'robust' as the decrease in $^{12}C^-$ counts was caused by a minor drop in the primary beam intensity. In general, lower secondary count rates indicate analysis of porous domains, whereas higher $^{12}C^-$ count rates are mainly associated with epoxy (and/or other phases) overlapping the analysis pit.

In the second session (August 2012), we included the simultaneous measurement of $^{13}CH^-$ with $^{12}C^-$ and $^{13}C^-$ that provides an indication of water, organic matter content, and/or other H-bearing phases present in the SIMS pit that may compromise the quality of the data. The $^{13}CH/^{13}C$ ratio of each sample analysis is background-corrected by subtraction of the average $^{13}CH/^{13}C$ of the eight bracketing UWC-3 standard analyses (see Table S1 in the supporting information). During this session, all background-corrected $^{13}CH/^{13}C$ ratios were clustered in a relatively narrow range ($3.5x10^{-2}$ to $8.3x10^{-3}$), and measured $\delta^{13}C$ is not correlated with $^{13}CH/^{13}C$. Thus, no data was excluded from the dataset based on elevated $^{13}CH/^{13}C$ ratios.

After ion microprobe measurements, all SIMS analysis pits were imaged by SEM to verify their exact location and to identify 'irregular' pits (Cavosie et al., 2005). Carbon isotope data from spots overlapping epoxy resin or areas of high porosity in the foraminifer chamber walls were not used.

3 Results

Comparison of published $\delta^{13}C$ values measured from pooled, multi-shell samples (multi-shell $\delta^{13}C_{GSMS}$) of *M. velascoensis* (Bralower et al., 1995b) to those measured by $\delta^{13}C_{SIMS}$ analyses in shells of *M. velascoensis* and *M. allisonensis* (Table 1) shows that both datasets record the negative CIE in the hole 865C PETM section, but the magnitude of the CIE differs between the two parallel records (Fig. 1B). The $\delta^{13}C_{SIMS}$ values acquired from shells of pre-CIE *M. velascoensis* are centered on ~4.7‰ (VPDB; n = 9 shells) and slightly higher than correlative multi-shell $\delta^{13}C_{GSMS}$ values. However, the sign of the difference between $\delta^{13}C_{SIMS}$ and multi-shell $\delta^{13}C_{GSMS}$ values is reversed within the CIE interval (~103.00 – 102.80 mbsf) where $\delta^{13}C_{SIMS}$ values for the PETM taxon *M. allisonensis* (~0.1‰ VPDB, n = 4 shells) are ~2‰ lower than corresponding multi-shell $\delta^{13}C_{GSMS}$ values for *M. velascoensis*. Within the overlying post-CIE interval (102.00 – 101.30 mbsf), both multi-shell $\delta^{13}C_{GSMS}$ and $\delta^{13}C_{SIMS}$ values of *M. velascoensis* (~4.5‰ VPDB, n = 4 shells) return to near pre-CIE values, and the original relation where $\delta^{13}C_{SIMS}$ values are higher

than correlative multi-shell $\delta^{13}C_{GSMS}$ values for *M. velascoensis* is reestablished (Fig. 1B). Thus, the mean magnitude of the excursion (~4.6‰) recorded by the $\delta^{13}C_{SIMS}$ data is ~2‰ larger than the CIE recorded by correlative multi-shell $\delta^{13}C_{GSMS}$ values, with the total range from highest to lowest $\delta^{13}C_{SIMS}$ values approaching ~6‰ (Fig. 1B).

The differences between the SIMS and GSMS $\delta^{13}C$ datasets are further investigated by plotting the $\delta^{13}C_{SIMS}$ values against previously reported (Kelly et al., 1996; Kelly et al., 1998) $\delta^{13}C_{GSMS}$ values measured from individual shells of *M. velascoensis* and *M. allisonensis* from within the CIE interval of hole 865C (Fig. 3). We make this comparison because, unlike the multi-shell $\delta^{13}C_{GSMS}$ record, the "single-shell" $\delta^{13}C_{GSMS}$ record includes values measured from individual shells of the PETM taxon, *M. allisonensis*. Hence, we are able to directly compare the $\delta^{13}C_{SIMS}$ and single-shell $\delta^{13}C_{GSMS}$ values for *M. allisonensis*. Yet, despite the inclusion of single-shell $\delta^{13}C_{GSMS}$ values for *M. allisonensis*, the results of this comparison are similar to those described above for the comparison to multi-shell $\delta^{13}C_{GSMS}$ values. Namely, the CIE interval is characterized by a reversal in the sign of the relation between *in situ* $\delta^{13}C_{SIMS}$ and single-shell $\delta^{13}C_{GSMS}$ values registered by *M. allisonensis*, with the CIE magnitude delimited by the single-shell $\delta^{13}C_{GSMS}$ values still being ~2‰ smaller than the mean CIE magnitude recorded by $\delta^{13}C_{SIMS}$ values (Fig. 3).

The $\delta^{13}C_{SIMS}$ values of the diagenetic crystallites are centered on ~2.8‰ (Fig. 2B) and similar to the multi-shell $\delta^{13}C_{GSMS}$ values of *M. velascoensis* samples from within the CIE interval of hole 865B (Fig. 1B). In contrast, the mean $\delta^{13}C_{SIMS}$ composition of the diagenetic crystallites falls between the single-shell $\delta^{13}C_{GSMS}$ values of pre-CIE and CIE morozovellid shells (Fig. 3). We also note that the mean $\delta^{13}C_{SIMS}$ composition of these blocky crystallites (~2.8‰ VPDB, $n = 4$ crystallites) is comparable to that of a smaller crystallite (~3.2‰ VPDB) found inside an *M. allisonensis* shell from the CIE interval (102.86 mbsf) of hole 865C (Figs. 2B, C, D).

4 Discussion

The integrity of PETM records recovered from the deep-sea sedimentary archive has been questioned on the grounds that the stratigraphies have been distorted and/or rendered incomplete by the combined effects of such processes as carbonate dissolution (Zachos et al., 2005), sediment mixing (Ridgwell, 2007), and varying sedimentation rates (Kirtland Turner and Ridgwell, 2013). In addition, environmental change wrought by the PETM induced biotic responses that involved faunal change and physiological ("vital") effects, which further complicate $\delta^{13}C$ records of the CIE (e.g., Bralower and Self- Trail, 2016; Thomas, 2003; Uchikawa and Zeebe, 2010). The combined effects of these processes are undoubtedly responsible for some of the disparities seen between the CIE magnitudes of terrestrial and marine sedimentary records (McInerney and Wing, 2011). Of particular interest to this study is the CIE magnitude (~3-4‰) returned

by planktic foraminifers (e.g., Gutjahr et al., 2017; Nunes and Norris, 2006; Zachos et al., 2003), which is ~2‰ smaller than that recorded by terrestrial organic and inorganic carbon (e.g., Bowen et al., 2001; Handley et al., 2008; Pagani et al., 2006). Moreover, the CIE magnitude delimited by $\delta^{13}C_{GSMS}$ values of mixed layer-dwelling planktic foraminifers varies spatially. For instance, the CIE compiled from published $\delta^{13}C_{GSMS}$ data approaches ~3‰ at Site 865 (Bralower et al., 1995b; Kelly et al., 1996), while it is ~4‰ at Sites 689 and 690 in the South Atlantic (Kennett and Stott, 1991; Zachos et al., 2007). To a degree, such variability may reflect spatial differences in primary productivity (i.e. biological pump) and sedimentation rates that affect the stratigraphic expression of the CIE (e.g., Kirtland Turner and Ridgwell, 2013; Sluijs et al., 2007; Thomas and Shackleton, 1996). Still, the size of the CIE recorded by 'whole-shell' $\delta^{13}C_{GSMS}$ measurements of planktic foraminifers from Site 865 falls at the lower end of the spectrum, and is substantially smaller than the CIE reported for terrestrial records. Below, we use the $\delta^{13}C$ data at hand to assess the potential of the aforementioned mechanisms to mask the full size of the CIE at Site 865 and, by the same token, arrive at the conclusion that post-depositional diagenesis is the most parsimonious explanation for the smaller CIE previously reported from Site 865.

Sediment-mixing processes such as winnowing by bottom-water currents and bioturbation have long been recognized as a means of smoothing marine chemostratigraphies, and the time-averaging effects of sediment mixing are especially problematic for multi-shell $\delta^{13}C_{GSMS}$ records compiled from measurements of aggregate (pooled) samples consisting of multiple foraminifer shells (e.g., Kirtland Turner and Ridgwell, 2013). The bimodal distribution of the single-shell $\delta^{13}C_{GSMS}$ values within the CIE interval of hole 865C (Kelly et al., 1996) attests to how sediment mixing has thoroughly blended this condensed PETM stratigraphy (Fig. 3). On the other hand, these same single-shell $\delta^{13}C_{GSMS}$ data can be used to reduce the effects of sediment mixing because the $\delta^{13}C$ signatures of individual shells clearly distinguish reworked pre-CIE shells with high $\delta^{13}C$ values from CIE shells with anomalously low $\delta^{13}C$ values. The efficacy of this "taphonomic filter" is evidenced by previous studies that have used single-shell $\delta^{13}C_{GSMS}$ values to show that none of the shells belonging to the thermocline-dwelling genus *Subbotina* spp. return a CIE value at Site 865 (Kelly et al., 1996; Kelly et al., 1998). This finding indicates that the vast majority of subbotinid shells found within the CIE interval at Site 865 are displaced contaminants from older sediments, and is why a complementary $\delta^{13}C_{SIMS}$ record for this thermocline-dwelling group was not generated in this study. Additionally, this same series of single-shell $\delta^{13}C_{GSMS}$ analyses revealed that the PETM taxon *M. allisonensis* ($n = 44$ shells) invariably yields anomalously low values thereby confirming that this distinctive morphotype lived only during the CIE (Kelly et al., 1996). Hence, single-shell $\delta^{13}C_{GSMS}$ values of planktic foraminifers – especially those of *M. allisonensis* – mitigates the effects of sediment mixing, yet these same single-shell $\delta^{13}C_{GSMS}$ values still yield a CIE magnitude of only ~2.6‰ (see Fig. 3).

Another potential mechanism for attenuating the CIE is changing ocean pH. Culturing experiments have shown that the stable isotope composition of modern planktic foraminifer shells is influenced by

seawater pH, with $\delta^{13}C$ values increasing at lower pH levels (Spero et al., 1997). This revelation has fueled speculation that ocean acidification may have increased the $\delta^{13}C$ of planktic foraminifer shells during the PETM, thereby reducing the size of the recorded excursion (Pagani et al., 2006). Modeling of this pH effect indicates that the $\delta^{13}C$ of mixed layer-dwelling morozovellids may have been increased by as much as ~0.9‰ during the PETM (Uchikawa and Zeebe, 2010). However, if pH was the main driver in attenuating the CIE magnitude recorded by planktic foraminifers then the $\delta^{13}C_{SIMS}$ and single-shell $\delta^{13}C_{GSMS}$ values for the excursion taxon *M. allisonensis* should be roughly the same, yet this is clearly not the case (Fig. 3). This observation contradicts the notion that the difference between SIMS- and GSMS-based $\delta^{13}C$ values is due to changing ocean pH, but it does not preclude the possibility that a pH-induced increase in planktic foraminifer $\delta^{13}C$ compositions may have dampened the overall amplitude of the CIE recorded by our $\delta^{13}C_{SIMS}$ analyses. Taking this provision into account suggests that the actual size of the CIE in the surface DIC reservoir may have been on the order of ~5-6‰. We therefore consider the ~4.6‰ excursion seen in our $\delta^{13}C_{SIMS}$ record to be a conservative estimate of the full CIE for the surface DIC reservoir.

Virtually all deep-sea PETM records feature a decline in sedimentary calcite that typically manifests as a clay-rich layer coincident with the CIE onset (e.g., Zachos et al., 2005). This drop in the amount of sedimentary calcite signals a transient increase in carbonate dissolution in response to carbon input during the initial stages of the PETM (Dickens et al., 1997). Detailed study of PETM sections arrayed along a bathymetric transect has shown that resultant shoaling of the calcite compensation depth (CCD) truncated the basal stratigraphies of these PETM records, which in turn reduced the magnitude of the CIE (e.g., Zachos et al., 2005; McCarren et al., 2008). Thus, it has been argued that carbonate dissolution has rendered many deep-sea PETM records incomplete (Pagani et al., 2006). This same line of reasoning has been used to explain the larger CIEs (~6-8‰) returned by bulk-carbonate $\delta^{13}C_{GSMS}$ records generated for PETM sections deposited in neritic settings that presumably remained well above the CCD and were not strongly affected by carbonate dissolution (Zhang et al., 2017). Although a clay-rich dissolution layer is not observed at Site 865, we assume *a priori* that both PETM records at Site 865 have been truncated by carbonate dissolution given the global extent of ocean acidification (Penman et al., 2014; Zeebe et al., 2009) and absence of intermediate (transitional) values in the single-shell $\delta^{13}C_{GSMS}$ data set (Kelly et al., 1996). We therefore have good reason to suspect that the stratigraphies of the Site 865 PETM records do not capture the full CIE, which is yet another reason to consider our SIMS-based excursion to be a minimum estimate of the true CIE magnitude. This said, we do not consider dissolution to be the cause of the observed differences between the $\delta^{13}C_{SIMS}$ and single-shell $\delta^{13}C_{GSMS}$ values because none of the shells examined/analyzed in this study show signs of significant dissolution.

Having evaluated the feasibility of these alternative mechanisms, we examine the $\delta^{13}C$ data through the lens of post-depositional diagenesis. All planktic foraminifer shells analyzed in this study appear “frosty” (opaque, stark white) under reflected light and possess protuberances (muricae) on the exterior surface of

their shells that have been thickened into blade-like structures (see Figs. 2E, F). These are the telltale signs of diagenesis (Sexton et al., 2006). Moreover, SEM imaging of planktic foraminifer shells has confirmed that carbonate recrystallization is pervasive throughout the entirety of the early Paleogene section recovered at Site 865 (Edgar et al., 2015; Pearson and Burgess, 2008; Sexton et al., 2006). In short, the morozovellid shells analyzed in this study feature a strong diagenetic overprint.

In an effort to reduce the effects of diagenesis, an earlier study used *in situ* $\delta^{18}O_{SIMS}$ measurements on isolated domains within individual morozovellid shells from the Site 865 PETM section (Kozdon et al., 2013). These ultra-high resolution (~3-μm analysis pits) $\delta^{18}O_{SIMS}$ analyses revealed that the relatively non-porous domain located at the base of muricae is better preserved than the rest of the shell, and that this same domain, at the very least, partially retains the original chemistry of the biogenic calcite (Kozdon et al., 2013). Thus, by targeting these same domains with $\delta^{13}C_{SIMS}$ analyses (Figs. 2E-F), we were able to prescribe a 'biogenic' endmember $\delta^{13}C$ value of 0.1‰ for *M. allisonensis* shells. This biogenic endmember $\delta^{13}C$ value was used, in combination with the diagenetic endmember $\delta^{13}C$ value of 2.8‰ measured from the crystallites as well as published $\delta^{18}O_{SIMS}$ data acquired from similar domains within *M. allisonensis* shells and the diagenetic crystallites (Kozdon et al., 2011, 2013), to construct a self-consistent mass balance for both carbon and oxygen isotopes (Fig. 4). The differences between the single-shell GSMS values and SIMS *in situ* measurements of both the biogenic and diagenetic compositional endmembers indicates that morozovellid shells from the hole 865C PETM section comprise about 45-55 wt.% diagenetic calcite, either through partial recrystallization of the shell or the addition of diagenetic cements. This degree of alteration closely matches earlier models for diagenesis in deep-sea sediments that estimate ~30 wt.% recrystallization and/or cementation (Schrag et al., 1995; Schrag, 1999; Tripati et al., 2003) as well as an earlier mass balance based solely on $\delta^{18}O$ measurements (Kozdon et al., 2011). The results of our mass balance calculations support the view that the foraminifer shells analyzed in this study are an aggregate mixture of both biogenic and diagenetic calcites, and that the subdomains targeted by SIMS are better preserved than the rest of the shell. Given the degree of alteration, and that the two carbonate phases formed under very different geochemical conditions, we posit that post-depositional diagenesis is the primary agent for attenuating the CIE recorded by $\delta^{13}C_{GSMS}$ analyses of whole planktic foraminifer shells.

A highly relevant aspect of the $\delta^{13}C$ data is the reversal of the $\delta^{13}C_{SIMS}$ vs. $\delta^{13}C_{GSMS}$ relation across the CIE interval (Figs. 1B, 3), which contradicts the view that the offsets in $\delta^{13}C$ reflect a systematic bias between the two analytical techniques. One possibility is that $\delta^{13}C$ offsets between SIMS and GSMS analyses are due to a combination of intra-shell $\delta^{13}C$ variation and the differing amounts of material analyzed by the two techniques. For instance, <1 ng of material is analyzed with a 7-μm SIMS spot, whereas a whole-shell GSMS measurement carried out on an individual shell (300-355 μm in diameter) typically analyzes ~20 μg of calcite. Thus, the $\delta^{13}C$ offsets could be due to the measurement of ^{13}C-depleted juvenile chambers by whole-shell GSMS analyses that are excluded from SIMS analyses entailing *in situ* $\delta^{13}C$

measurements in isolated subdomains of a shell. This explanation is plausible for the pre- and post-CIE intervals where $\delta^{13}C_{SIMS}$ values are higher than correlative $\delta^{13}C_{GSMS}$ values, but it does not account for the reversal in the SIMS vs. GSMS relation registered by *M. allisonensis* shells within the CIE interval (Fig. 3). To address this inconsistency, we consider an auxiliary hypothesis positing that the loss of algal photosymbionts hosted by many planktic foraminifer species (i.e. symbiont bleaching) led to a transient loss of the $\delta^{13}C$/size relation within *M. allisonensis* during the PETM (e.g., Si and Aubry, 2018). In essence, symbiont bleaching would result in a breakdown of the $\delta^{13}C$/size relation thereby reducing inter-chamber $\delta^{13}C$ variation within a shell by removing the ^{13}C-enriched signal associated with larger, adult chambers. Symbiont bleaching warrants consideration owing to the extreme environmental conditions of the PETM, but we do not favor this interpretation because GSMS-based stable isotope analyses of size-segregated samples have shown that the PETM taxon, *M. allisonensis*, retains this $\delta^{13}C$/size relation at Site 865 (Kelly et al., 1998). In addition, a loss of the $\delta^{13}C$/size relation would amplify – not attenuate – the CIE, which would suggest that the negative excursion observed in planktic foraminifer $\delta^{13}C$ records overestimates the true size of the CIE. Hence, symbiont bleaching does not address the problem at hand; that being, why is the CIE in planktic foraminifer records smaller relative to that of terrestrial records? Finally, a reduction in intra-shell $\delta^{13}C$ variability should bring the *in situ* $\delta^{13}C_{SIMS}$ and whole-shell $\delta^{13}C_{GSMS}$ values into agreement. Yet, to the contrary, $\delta^{13}C_{SIMS}$ values are 1.2‰ lower than single-shell $\delta^{13}C_{GSMS}$ values for *M. allisonensis* within the CIE interval (Fig. 3).

To gain insight into the reversal of the $\delta^{13}C_{SIMS}$ vs. $\delta^{13}C_{GSMS}$ relation, we turn our attention back to the $\delta^{13}C_{SIMS}$ values measured from the diagenetic crystallites. The mean $\delta^{13}C_{SIMS}$ composition of these crystallites (2.8‰ VPDB) is comparable to that measured from the crystallite (3.2‰) found inside a *M. allisonensis* shell from the hole 865C section (Figs. 2B, C, D), so we assume that the $\delta^{13}C$ composition of the crystallites is representative of the $\delta^{13}C$ of the secondary calcite overprinting foraminifer shells within the CIE interval. More importantly, the average $\delta^{13}C_{SIMS}$ value of the crystallites is centered between single-shell $\delta^{13}C_{GSMS}$ values returned by pre-CIE and CIE morozovellids (Fig. 3). The intermediate $\delta^{13}C$ values of the crystallites suggest that post-depositional diagenesis increases the whole-shell $\delta^{13}C_{GSMS}$ values of CIE foraminifers. We therefore posit that the addition of diagenetic calcite increased whole-shell $\delta^{13}C_{GSMS}$ values of CIE *M. allisonensis* making them ^{13}C-enriched relative to corresponding *in situ* $\delta^{13}C_{SIMS}$ values ($\delta^{13}C_{SIMS} < \delta^{13}C_{GSMS}$). The end result would be the observed reversal in $\delta^{13}C_{SIMS}$ vs. $\delta^{13}C_{GSMS}$ values within the CIE interval (Fig. 3), and the attenuation of the CIE by a diagenetic process that shifted the whole-shell $\delta^{13}C$ compositions of CIE foraminifers toward the intermediate $\delta^{13}C$ composition of the crystallites. An interesting corollary is that post-depositional diagenesis has the potential to alter the whole-shell $\delta^{13}C$ compositions of **all** planktic foraminifers (i.e. pre-CIE and CIE shells) preserved within the CIE interval. Hence, it is likely that post-depositional diagenesis attenuates the CIE magnitude by, not only increasing

the $\delta^{13}C$ compositions of CIE shells, but also by decreasing the $\delta^{13}C$ compositions of pre-CIE shells that were reworked up-section into the CIE interval prior to cementation.

The stratigraphic distribution of the crystallites is restricted to the CIE interval of hole 865B, suggesting that their formation was penecontemporaneous with sediment deposition/mixing during the PETM (Kozdon et al., 2013). Based on current understanding of carbonate saturation history for the PETM, the stratigraphic distribution of crystallites reflects the precipitation of secondary carbonate that overprinted the PETM section during the later (i.e. recovery) stages of the CIE. Initial carbon input resulted in carbonate undersaturation, which fueled dissolution of previously deposited pre-CIE calcite with high $\delta^{13}C$ compositions both on the sea floor and within the upper part of the sediment column, as well as the remineralization of biogenic calcite with low $\delta^{13}C$ compositions that precipitated during the earliest stages of the CIE (e.g., Bralower et al., 2014; Dickens, 2000; Zachos et al., 2005). This short-lived episode of "chemical erosion" was followed by a period of carbonate oversaturation driven by the enhancement of such negative feedbacks as silicate mineral weathering reactions during the recovery phase of the CIE (e.g., Kelly et al., 2005; Penman et al., 2016). Thus, the CIE recovery is typified by CCD subsidence to water depths in excess of the bathymetric position it held prior to carbon input and the widespread preservation of sedimentary calcite on the sea floor (e.g., Penman et al., 2016). We therefore argue that the crystallites formed during the CIE recovery as the carbonate saturation state of the ocean increased. Further, we posit that this "overshoot" in carbonate saturation fostered crystallite formation through the reprecipitation of inorganic carbon dissolved within sedimentary pore fluids. Thus, the intermediate $\delta^{13}C$ values of the crystallites (~2.8‰) indicate that these diagenetic cements are an amalgamated blend of two carbonate phases with distinctly different $\delta^{13}C$ compositions – pre-CIE 'donor' carbonate and ambient CIE carbonate dissolved in bottom waters – that reprecipitated to overprint the PETM record at Site 865 (Kozdon et al., 2013). This view is supported by the similar $\delta^{13}C$ compositions of the crystallites and correlative pooled, multi-shell samples as the latter are themselves mixtures of foraminifer shells with pre-CIE and CIE $\delta^{13}C$ compositions (Fig. 1B).

Although we consider our revised CIE magnitude of ~4.6‰ to be a conservative estimate of the full CIE in the surface DIC reservoir, it is congruent with the mean CIE magnitude compiled from terrestrial records. To a first approximation, mass balance calculations (McInerney and Wing, 2011) using a CIE of 4.6‰ for surface DIC requires the release of either ~4,300 Pg of C from marine sedimentary methane hydrates ($\delta^{13}C$ = -60‰), ~10,000 Pg of C from thermogenic methane or Antarctic permafrost ($\delta^{13}C$ = -30‰), or the oxidation of ~15,400 Pg of organic matter ($\delta^{13}C$ = -22‰). A total release of ~4,300 Pg of methane carbon ($\delta^{13}C$ = -60‰) is grossly similar to that used to reproduce observed patterns of carbonate dissolution in global ocean during the PETM (Zeebe et al., 2009). When viewed within the context of model simulations run for a range of carbon input durations (Kirtland Turner and Ridgwell, 2016), our revised CIE is most consistent with scenarios entailing shorter (≤5 kyr) carbon input durations sourced by biogenic methane

($\delta^{13}C$ = -60‰) and/or organic matter ($\delta^{13}C$ = -22‰). However, we note that such estimates for mass and rate of carbon input are deemed provisional, and are meant to motivate future modeling studies. This is especially the case in light of recently reported evidence suggesting that the CIE was caused by igneous activity related to the North Atlantic Igneous Province (e.g., Storey et al., 2007), and that the CIE reflects a more sustained (~55 kyr) release of even greater amounts (~10,200-12,200 Pg C) of isotopically heavier carbon ($\delta^{13}C$ = -11‰ to -17‰) sourced by mantle CO_2 outgassing and thermal combustion of organic matter (Gutjahr et al., 2017).

5 Conclusions

SIMS-based *in situ* measurements of $\delta^{13}C$ in minute (~7-μm diameter) domains within individual shells of mixed layer-dwelling planktic foraminifers yield a CIE magnitude (~4.6‰) that is ~2‰ larger than that registered by conventional 'whole shell' GSMS measurements of the same planktic foraminifer species in the PETM record recovered at Site 865. The transient reversal in the sign of the SIMS vs. GSMS $\delta^{13}C$ relation within the CIE interval, where $\delta^{13}C_{SIMS}$ values are lower than those of correlative $\delta^{13}C_{GSMS}$ measurements, indicates that the larger CIE returned by SIMS analyses is not an artifact of a systematic analytical bias. Moreover, the intermediate $\delta^{13}C$ composition of crystallites found within the CIE interval suggests that the composition of these cements is an amalgamated blend of pre-CIE and CIE inorganic carbon; hence, post-depositional diagenesis has the potential to lower and increase whole-shell $\delta^{13}C_{GSMS}$ values measured from pre-CIE and CIE foraminifers, respectively. We therefore attribute the smaller CIE recorded by whole-shell $\delta^{13}C_{GSMS}$ values to post-depositional diagenesis shifting both pre-CIE and CIE whole-shell $\delta^{13}C_{GSMS}$ values towards the intermediate $\delta^{13}C$ composition of the diagenetic calcite. The "dual effects" of this diagenetic process are most applicable to carbonate-rich PETM records that have suffered chemical erosion of preexisting (pre-CIE) sedimentary calcite. Despite being ~2‰ larger than the CIE measured by GSMS, we consider our SIMS-based CIE of ~4.6‰ to be a conservative estimate of the full CIE in the surface DIC reservoir for two reasons. First, the domains targeted for *in situ* analysis may not be pristinely preserved, so our $\delta^{13}C_{SIMS}$ record likely underestimate the actual size of the CIE. Secondly, other processes not accounted for in this study such as a pH effect on foraminifer $\delta^{13}C$ compositions and truncation of the CIE stratigraphy by carbonate dissolution have likely conspired with post-depositional diagenesis to attenuate the CIE at Site 865. Nevertheless, we consider the larger excursion returned by SIMS $\delta^{13}C$ analysis to be a more accurate measure of the actual size of the CIE in the surface ocean, and we note that it is congruent with the mean CIE compiled from terrestrial PETM records reflecting the $\delta^{13}C$ of atmospheric CO_2. Similar studies geared toward constructing new SIMS-based $\delta^{13}C$ records of the CIE using other foraminifer taxa (i.e. mixed layer-dwelling acarininids, thermocline-dwelling subbotinids, and deep-sea benthics) from different deep-sea PETM sections are underway. Whether the diagenetic model

herein envisioned played a role in attenuating the CIEs marking other hyperthermal climate states entailing intensified carbonate dissolution is presently unknown.

Acknowledgments

This research was supported by NSF-OCE 1405224 to D.C.K and R.K. The UW-Madison Graduate School Competition provided bridge funds to D.C.K. This research used samples provided by the International Ocean Discovery Program (IODP). WiscSIMS is supported by NSF (EAR 1355590) and UW – Madison. Noriko Kita helped to perform SIMS analyses. Jim Kern provided assistance for general lab work. Sample mounts were prepared by Brian Hess. John Fournelle provided assistance for SEM imaging.

Availability of Data

A detailed data table (Table S1) can be downloaded from the supporting information.

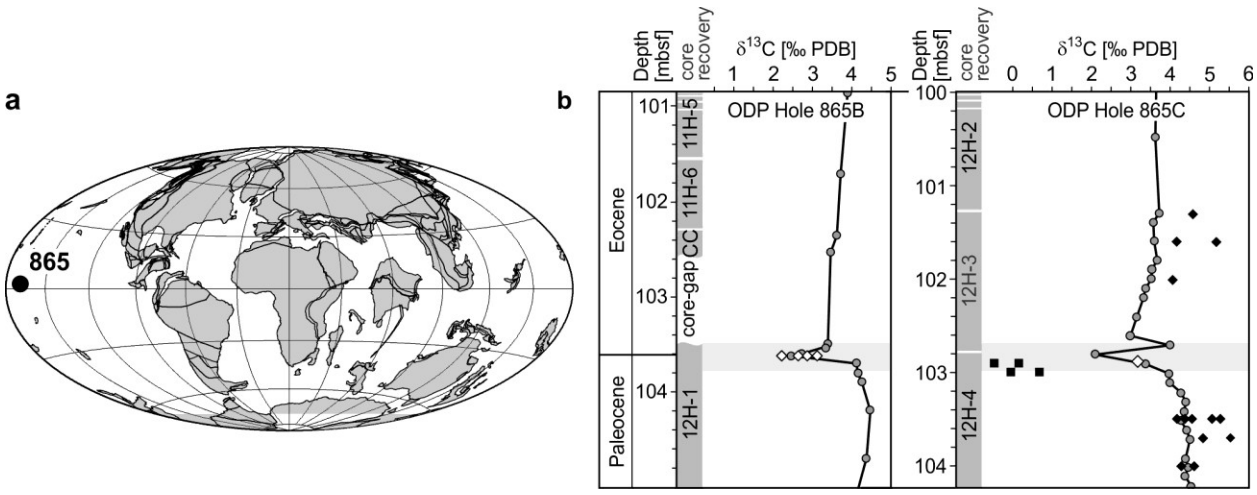

Figure 1. (**a**) Map showing early Eocene paleogeography (http://www.odsn.de) and location of Site 865. (**b**) Chemostratigraphic correlation of the hole 865B and 865C PETM sections using the CIE recorded by gas-source mass spectrometry (GSMS) of pooled, "multi-shell" samples (grey circles) of mixed layer-dwelling morozovellids (Bralower et al., 1995a). Mean SIMS-based $\delta^{13}C$ values measured *in situ* from subdomains of individual shells of *M. velascoensis* (black diamonds) and *M. allisonensis* (black squares) plotted against the published CIE record for the hole 865C section. Note diagenetic crystallites and calcite infilling chambers of *M. allisonensis* (open diamonds) are restricted to the CIE interval of holes 865B and 865C (grey bands), and that their $\delta^{13}C$ compositions are similar to those of correlative multi-shell samples measured by GSMS.

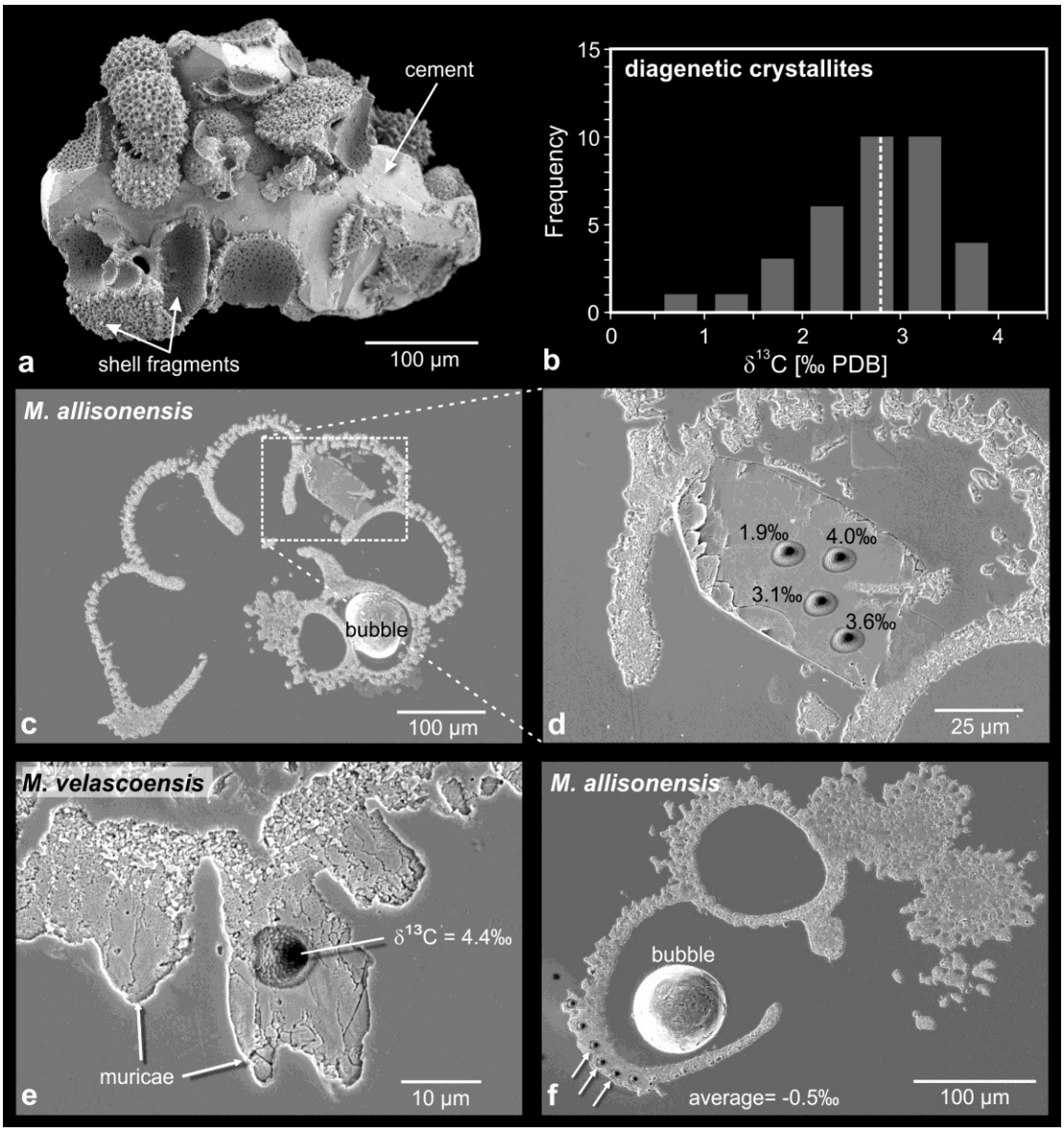

Fig. 2. (**a**) SEM image of diagenetic crystallite cementing foraminifer shells from the CIE interval (hole 865B, 103.60 mbsf). (**b**) Histogram showing frequency distribution of 35 *in situ* $\delta^{13}C$ measurements placed in four crystallites. Vertical dashed line denotes mean $\delta^{13}C$ composition of crystallites. (**c**) SEM image of a diagenetic crystallite (dashed box), polished to mid-section, found inside the chamber of the PETM morphotype *M. allisonensis* (hole 865C, 102.86 mbsf). (**d**) Enlarged image of crystallite shown in panel C with 7-µm SIMS analysis pits and corresponding $\delta^{13}C$ values. (**e**) SEM image of cross section through the chamber wall of *M. velascoensis* (865C, 12-4, 70-72 cm, 103.50 mbsf) showing placement of SIMS analysis pit near base of muricae blade and corresponding $\delta^{13}C$ value. (**f**) SEM image of a cross section through a shell of *M. allisonensis* (865C, 12-4, 10-12 cm, 102.90 mbsf) showing six SIMS analysis pits in the final chamber. The average $\delta^{13}C$ of three measurements is -0.5‰ (pits marked by arrows), the other pits were placed in domains impregnated by epoxy and were not used.

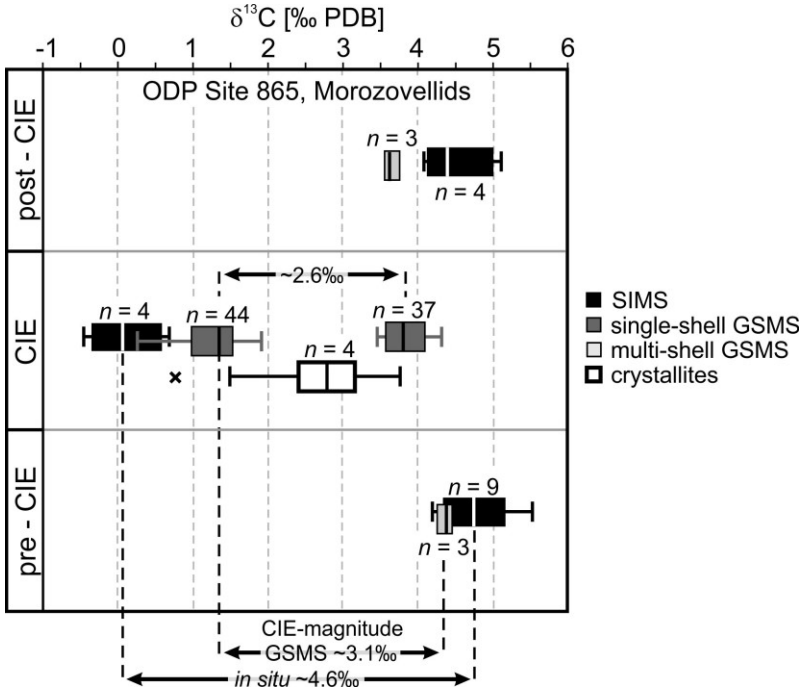

Fig. 3. Box and whisker plot summarizing differences in the magnitude of the carbon isotope excursion (CIE) between mean SIMS $\delta^{13}C$ values of individual morozovellid shells and conventional gas-source mass spectrometer (GSMS) analyses of pooled (multi-shell) and individual (single-shell) morozovellid samples. Boxes denote the first and the third quartiles, with the vertical line inside the box being the median value and whiskers delimiting the minimum and maximum of all $\delta^{13}C$ values for each dataset from the pre-CIE, CIE, and post-CIE intervals. Multi-shell $\delta^{13}C$ values (Bralower et al., 1995a) are from same pre- and post-CIE core samples as SIMS $\delta^{13}C$ values, all single-shell GSMS $\delta^{13}C$ values (Kelly et al., 1996) are from samples within CIE interval. Bimodal distribution of single-shell GSMS $\delta^{13}C$ values within CIE interval reflects sediment mixing. Note that SIMS-based CIE (4.6‰) is larger than that measured by GSMS analyses of multi-shell (~3.1‰) and single-shell (2.6‰) samples. SIMS $\delta^{13}C$ values for diagenetic cements (crystallites) from CIE interval are intermediate ($\delta^{13}C$ = 2.8‰) between mean GSMS $\delta^{13}C$ values of individual pre-CIE and CIE shells. Unusually low $\delta^{13}C$ value from an individual SIMS pit in a crystallite denoted by "x". Number (*n*) of multi-shell samples analyzed by GSMS, individual shells analyzed by SIMS or GSMS, and diagenetic crystallites analyzed by SIMS noted above/below corresponding boxes.

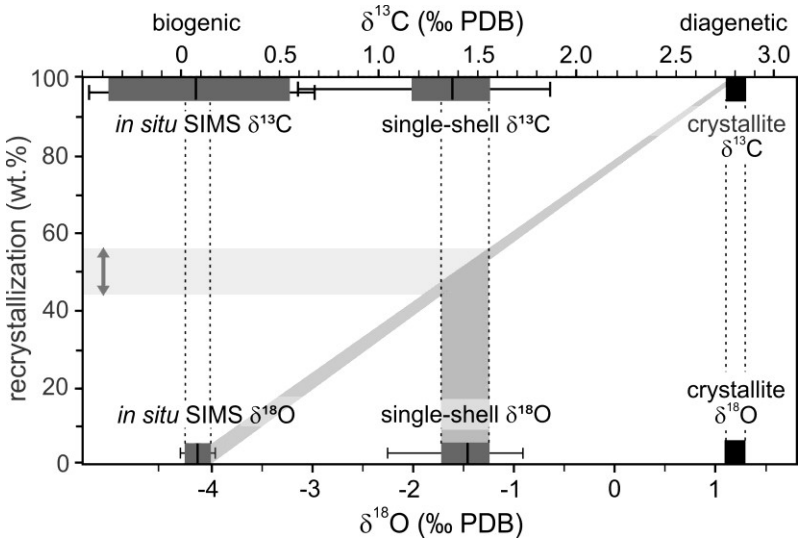

Fig. 4. Four-endmember mass-balance quantifying the degree of recrystallization for planktic foraminifer shells in the PETM records at Site 865. Mean values for SIMS-based $\delta^{13}C$ and $\delta^{18}O$ compositions of crystallites represent the diagenetic endmembers, while the range and median of SIMS-based $\delta^{13}C$ and $\delta^{18}O$ values measured *in situ* from individual shells of the PETM-morphotype *M. allisonensis* delimit the 'biogenic' endmembers. Note that $\delta^{13}C$ and $\delta^{18}O$ values for individual shells of *M. allisonensis* (Kelly et al., 1996), as determined by conventional gas-source mass spectrometry (GSMS), fall between the diagenetic and 'biogenic' endmember values, indicating that the whole-shell isotope compositions are a mixture of the two carbonate phases. SIMS-based $\delta^{18}O$ values for *M. allisonensis* shells are from Kozdon et al. (2011), SIMS-based $\delta^{18}O$ values for the diagenetic crystallites are from Kozdon et al. (2013).

Table 1

In situ $\delta^{13}C$ *Analyses by Ion Microprobe in Morozovellid Species and Diagenetic Crystallites from ODP Site 865, Central Pacific*

***In situ* $\delta^{13}C$ analyses of foraminifera shells**								
Hole, core section, interval	MBSF [m]	Event	Species	Size fraction [µm]	Shell/analysis number	Individual $\delta^{13}C$ analysis [‰ PDB]	± 2 SD [a]	$\delta^{13}C$, mean of each shell [‰ PDB]
865C, 12-3, 0-2cm	101.30	post-CIE	*M. velascoensis*	300 - 355	Shell 80-1	5.42	1.02	4.57
					Shell 80-2	4.35	1.02	
					Shell 80-3	3.93	1.02	
865C, 12-3, 30-32 cm	101.60	post-CIE	*M. velascoensis*	300 - 355	Shell 117-1	3.65	0.66	4.16
					Shell 117-2	4.66	0.66	
					Shell 115-1	3.45	0.53	5.13
					Shell 115-2	6.45	0.53	
					Shell 115-4	4.59	0.53	
					Shell 115-5	4.87	0.53	
					Shell 115-7	6.27	0.53	
865C, 12-3, 70-72 cm	102.00	post-CIE	*M. velascoensis*	300 - 355	Shell 68-1	4.05	0.33	4.05
865C, 12-4, 10-12 cm	102.90	CIE	*M. allisonensis*	300 - 355	Shell 51-2	-0.19	0.45	-0.47
					Shell 51-3	-0.96	0.45	
					Shell 51-4	-0.25	0.45	
					Shell 52-1	-0.62	0.47	0.17
					Shell 52-2	1.41	0.47	
					Shell 52-3	0.13	0.47	
					Shell 52-4	-0.22	0.47	
					Shell 52-5	0.16	0.47	
865C, 12-4, 20-22 cm	103.00	CIE	*M. allisonensis*	300 - 355	Shell 17-1	0.69	0.47	0.69
					Shell 18-1	-0.78	0.47	-0.05
					Shell 18-2	0.68	0.47	
865C, 12-4, 70-72 cm	103.50	pre-CIE	*M. velascoensis*	300 - 355	Shell 12-1	5.43	0.59	4.52
					Shell 12-2	5.07	0.59	
					Shell 12-3	3.07	0.59	
					Shell 13-1	3.57	0.59	4.18
					Shell 13-3	4.79	0.59	
					Shell 14-1	4.23	0.55	4.37

					Shell 14-2	4.55	0.55	
					Shell 14-3	4.29	0.55	
					Shell 14-4	5.06	0.55	
					Shell 14-5	3.75	0.55	
					Shell 15-1	5.48	0.55	5.27
					Shell 15-2	4.92	0.55	
					Shell 15-4	5.40	0.55	
					Shell 16-1	4.41	0.55	5.03
					Shell 16-2	5.65	0.81	
865C, 12-4, 90-92 cm	103.70	pre-CIE	*M. velascoensis*	300 - 355	Shell 129-1	3.89	1.43	4.81
					Shell 129-2	5.67	1.43	
					Shell 129-3	4.87	1.43	
					Shell 127-1	6.10	1.43	5.51
					Shell 127-3	5.45	1.43	
					Shell 127-4	4.99	1.43	
865C, 12-4, 120-122 cm	104.00	pre-CIE	*M. velascoensis*	300 - 355	Shell 100-1	3.71	0.36	4.27
					Shell 100-2	3.84	0.36	
					Shell 100-3	5.23	0.36	
					Shell 100-4	4.30	0.36	
					Shell 103-1	2.37	0.36	4.60
					Shell 103-2	4.74	0.36	
					Shell 103-3	5.83	0.36	
					Shell 103-4	5.45	0.36	

***In situ* $\delta^{13}C$ analyses of diagenetic crystallites and chamber infilling**

Hole, core section, interval	MBSF [m]	Event	Species	Size fraction [µm]	Crystallite # and analysis number	Individual $\delta^{13}C$ analysis [‰ PDB]	± 2 SD [a]	$\delta^{13}C$, mean of each crystallite [‰ PDB]
865B, 12H-1, 10-12 cm	103.60	CIE			Crystallite #3, 1	1.91	0.79	2.23
					Crystallite #3, 2	1.81	0.79	
					Crystallite #3, 3	2.93	0.79	
					Crystallite #3, 4	2.85	0.79	
					Crystallite #3, 5	2.16	0.79	
					Crystallite #3, 6	3.48	0.79	
					Crystallite #3, 7	1.77	0.79	
					Crystallite #3, 8	2.52	0.79	

					Crystallite #3, 9	1.63	0.79	
					Crystallite #3, 10	2.62	0.79	
865B, 12H-1, 10-12 cm	103.60	CIE			Crystallite #5, 1	2.59	0.81	2.92
					Crystallite #5, 2	3.08	0.81	
					Crystallite #5, 3	2.87	0.81	
					Crystallite #5, 4	3.14	0.81	
865B, 12H-1, 10-12 cm	103.60	CIE			Crystallite #6, 1	2.75	0.60	2.64
					Crystallite #6, 2	3.06	0.60	
					Crystallite #6, 3	2.91	0.60	
					Crystallite #6, 4	3.23	0.60	
					Crystallite #6, 5	0.77	0.60	
					Crystallite #6, 6	2.78	0.60	
					Crystallite #6, 7	3.15	0.60	
					Crystallite #6, 8	2.46	0.60	
865B, 12H-1, 10-12 cm	103.60	CIE			Crystallite #7, 1	3.56	1.15	3.12
					Crystallite #7, 2	3.13	1.15	
					Crystallite #7, 3	3.16	1.15	
					Crystallite #7, 4	2.68	1.15	
					Crystallite #7, 5	3.37	1.15	
					Crystallite #7, 6	2.95	1.15	
					Crystallite #7, 7	2.26	1.15	
					Crystallite #7, 8	2.40	1.15	
					Crystallite #7, 9	3.77	1.15	
					Crystallite #7, 10	3.14	1.15	
					Crystallite #7, 11	2.71	1.15	
					Crystallite #7, 12	3.73	1.15	
					Crystallite #7, 13	3.74	1.15	
865C, 12-4, 6-8 cm	102.87	CIE	*M. allisonensis*	300 - 355	Shell 60, infilling, 1	1.88	1.04	3.16
					Shell 60, infilling, 2	3.13	1.04	
					Shell 60, infilling, 3	3.97	1.04	
					Shell 60, infilling, 4	3.64	1.04	

[a)] reproducibility, defined as the spot-to-spot reproducibility of the eight standard analyses bracketing each block of sample analyses

3

References

Bains, S., R. D. Norris, R. M. Corfield, G. J. Bowen, P. D. Gingerich, and P. L. Koch (2003), Marine-terrestrial linkages at the Paleocene-Eocene boundary, *Geol. Soc. Am. Spec. Pap.*, *369*, 1-9.

Böhm, F., A. Haase-Schramm, A. Eisenhauer, W. C. Dullo, M. Joachimski, H. Lehnert, and J. Reitner (2002), Evidence for preindustrial variations in the marine surface water carbonate system from coralline sponges, *Geochemistry, Geophysics, Geosystems*, *3*(3), 1-13.

Bowen, G. J., J. Koch, P. D. Gingerich, R. D. Norris, S. Bains, and R. M. Corfield (2001), Refined Isotope Stratigraphy Across the Continental Paleocene-Eocene Boundary on Polecat Bench in the Northern Bighorn Basin, in *Paleocene Eocene Stratigraphy and Biotic Change in the Bighorn and Clarks Fork Basins, Wyoming*, edited by P. D. Gingerich, pp. 73-88, University of Michigan Papers on Paleontology.

Bowen, G. J., D. J. Beerling, P. L. Koch, J. C. Zachos, and T. Quattlebaum (2004), A humid climate state during the Palaeocene/Eocene thermal maximum, *Nature*, *432*(7016), 495-499, doi:http://www.nature.com/nature/journal/v432/n7016/suppinfo/nature03115_S1.html.

Bralower, T. J., K. J. Meissner, K. Alexander, and D. J. Thomas (2014), The dynamics of global change at the Paleocene-Eocene thermal maximum: A data-model comparison, *Geochemistry, Geophysics, Geosystems*, *15*(10), 3830-3848.

Bralower, T. J., and J. M. Self- Trail (2016), Nannoplankton malformation during the Paleocene-Eocene Thermal Maximum and its paleoecological and paleoceanographic significance, *Paleoceanography*, *31*(10), 1423-1439.

Bralower, T. J., J. C. Zachos, E. Thomas, M. Parrow, C. K. Paull, D. C. Kelly, I. P. Silva, W. V. Sliter, and K. C. Lohmann (1995a), Late Paleocene to Eocene paleoceanography of the equatorial Pacific Ocean: Stable isotopes recorded at Ocean Drilling Program Site 865, Allison Guyot, *Paleoceanography*, *10*(4), 841-865.

Bralower, T. J., M. Parrow, E. Thomas, and J. C. Zachos (1995b), Data Report: Stable Isotopic Stratigraphy of the of the Paleogene pelagic cap at Site 865, Allison Guyot.*Rep.*, 581-586 pp, Ocean Drilling Program, College Station.

Cavosie, A. J., J. W. Valley, S. A. Wilde, and E.I.M.F (2005), Magmatic $\delta^{18}O$ in 4400–3900 Ma detrital zircons: A record of the alteration and recycling of crust in the Early Archean, *Earth Planet. Sci. Lett.*, *235*(3–4), 663-681, doi:10.1016/j.epsl.2005.04.028.

Cohen, A. S., A. L. Coe, and D. B. Kemp (2007), The Late Palaeocene–Early Eocene and Toarcian (Early Jurassic) carbon isotope excursions: a comparison of their time scales, associated environmental changes, causes and consequences, *Journal of the Geological Society*, *164*(6), 1093-1108, doi:10.1144/0016-76492006-123.

Craig, H. (1957), Isotopic standards for carbon and oxygen and correction factors for mass-spectrometric analysis of carbon dioxide, *Geochim. Cosmochim. Acta*, *12*(1–2), 133-149, doi:10.1016/0016-7037(57)90024-8.

Cramer, B. S., J. D. Wright, D. V. Kent, and M. P. Aubry (2003), Orbital climate forcing of δ13C excursions in the late Paleocene–early Eocene (chrons C24n–C25n), *Paleoceanography*, *18*(4).

Cui, Y., L. R. Kump, A. J. Ridgwell, A. J. Charles, C. K. Junium, A. F. Diefendorf, K. H. Freeman, N. M. Urban, and I. C. Harding (2011), Slow release of fossil carbon during the Palaeocene-Eocene Thermal Maximum, *Nature Geosci*, *4*(7), 481-485, doi:http://www.nature.com/ngeo/journal/v4/n7/abs/ngeo1179.html#supplementary-information.

Dickens, G. R., J. R. O'Neil, D. K. Rea, and M. Owen (1995), Dissociation of oceanic methane hydrate as a cause of the carbon isotope excursion at the end of the Paleocene., *Paleoceanography*, *10*, 965-971.

Dickens, G. R., M. M. Castillo, and J. C. G. Walker (1997), A blast of gas in the latest Paleocene: Simulating first-order effects of massive dissociation of oceanic methane hydrate, *Geology*, *25*(3), 259-262, doi:10.1130/0091-7613(1997)025<0259:abogit>2.3.co;2.

Dickens, G. R. (2000), Methane oxidation during the late Palaeocene thermal maximum, *Bull. Soc. Geol. Fr.*, *171*(1), 37-49.

Dickens, G. R. (2011), Down the Rabbit Hole: toward appropriate discussion of methane release from gas hydrate systems during the Paleocene-Eocene thermal maximum and other past hyperthermal events, *Clim. Past*, *7*(3), 831-846, doi:10.5194/cp-7-831-2011.

Edgar, K. M., E. Anagnostou, P. N. Pearson, and G. L. Foster (2015), Assessing the impact of diagenesis on $\delta^{11}B$, $\delta^{13}C$, $\delta^{18}O$, Sr/Ca and B/Ca values in fossil planktic foraminiferal calcite, *Geochim. Cosmochim. Acta*, *166*, 189-209, doi:http://dx.doi.org/10.1016/j.gca.2015.06.018.

Gingerich, P. D. (2006), Environment and evolution through the Paleocene-Eocene thermal maximum., *Trends Ecol. Evol.*, *21*(246-253).

Gutjahr, M., A. Ridgwell, P. F. Sexton, E. Anagnostou, P. N. Pearson, H. Pälike, R. D. Norris, E. Thomas, and G. L. Foster (2017), Very large release of mostly volcanic carbon during the Palaeocene-Eocene Thermal Maximum, *Nature*, *548*, 573-577.

Handley, L., P. N. Pearson, I. K. McMillan, and R. D. Pancost (2008), Large terrestrial and marine carbon and hydrogen isotope excursions in a new Paleocene/Eocene boundary section from Tanzania, *Earth Planet. Sci. Lett.*, *275*(1–2), 17-25, doi:http://dx.doi.org/10.1016/j.epsl.2008.07.030.

Higgins, J. A., and D. P. Schrag (2006), Beyond methane: Towards a theory for the Paleocene–Eocene Thermal Maximum, *Earth Planet. Sci. Lett.*, *245*(3–4), 523-537, doi:10.1016/j.epsl.2006.03.009.

Huber, B. T., and L. C. Sloan (2000), Climatic responses to tropical sea surface temperature changes on a "greenhouse" Earth, *Paleoceanography*, *15*, 443-450.

Kelly, D. C., T. J. Bralower, J. C. Zachos, I. P. Silva, and E. Thomas (1996), Rapid diversification of planktonic foraminifera in the tropical Pacific (ODP Site 865) during the late Paleocene thermal maximum, *Geology*, *24*(5), 423-426.

Kelly, D. C., T. J. Bralower, and J. C. Zachos (1998), Evolutionary consequences of the latest Paleocene thermal maximum for tropical planktonic foraminifera, *Palaeogeogr., Palaeoclimatol., Palaeoecol.*, *141*, 139-161.

Kelly, D. C., T. J. Bralower, and J. C. Zachos (2001), On the demise of the early Paleogene *Morozovella velascoensis* lineage: Terminal progenesis in the planktonic foraminifera., *Palaois*, *16*, 507-523.

Kelly, D. C., J. C. Zachos, T. J. Bralower, and S. A. Schellenberg (2005), Enhanced terrestrial weathering/runoff and surface ocean carbonate production during the recovery stages of the Paleocene-Eocene thermal maximum, *Paleoceanography*, *20*(4), PA4023, doi:10.1029/2005pa001163.

Kennett, J. P., and L. D. Stott (1991), Abrupt deep-sea warming, palaeoceanographic changes and benthic extinctions at the end of the Paleocene, *Nature*, *353*, 225-229.

Kirtland Turner, S., and A. Ridgwell (2013), Recovering the true size of an Eocene hyperthermal from the marine sedimentary record, *Paleoceanography*, *28*(4), 2013PA002541, doi:10.1002/2013pa002541.

Kirtland Turner, S., and A. Ridgwell (2016), Development of a novel empirical framework for interpreting geological carbon isotope excursions, with implications for the rate of carbon injection across the PETM, *Earth Planet. Sci. Lett.*, *435*, 1-13.

Kita, N. T., T. Ushikubo, B. Fu, and J. W. Valley (2009), High precision SIMS oxygen isotope analysis and the effect of sample topography, *Chem. Geol.*, *264*(1-4), 43-57, doi:10.1016/j.chemgeo.2009.02.012.

Koch, P. L., J. C. Zachos, and P. D. Gingerich (1992), Correlation between isotope records in marine and continental carbon reservoirs near the Palaeocene/Eocene boundary, *Nature*, *358*(6384), 319-322.

Kozdon, R., T. Ushikubo, N. T. Kita, M. Spicuzza, and J. W. Valley (2009), Intratest oxygen isotope variability in the planktonic foraminifer *N. pachyderma:* Real vs. apparent vital effects by ion microprobe, *Chem. Geol.*, *258*, 327-337, doi:10.1016/j.chemgeo.2008.10.032.

Kozdon, R., D. C. Kelly, N. T. Kita, J. H. Fournelle, and J. W. Valley (2011), Planktonic foraminiferal oxygen isotope analysis by ion microprobe technique suggests warm tropical sea surface

103 temperatures during the Early Paleogene, *Paleoceanography*, *26*(3), PA3206,
104 doi:10.1029/2010pa002056.
105 Kozdon, R., D. C. Kelly, K. Kitajima, A. Strickland, J. H. Fournelle, and J. W. Valley (2013), In situ $\delta^{18}O$
106 and Mg/Ca analyses of diagenetic and planktic foraminiferal calcite preserved in a deep-sea
107 record of the Paleocene-Eocene thermal maximum, *Paleoceanography*, *28*(3), 517-528,
108 doi:10.1002/palo.20048.
109 McCarren, H., E. Thomas, T. Hasegawa, U. Röhl, and J. C. Zachos (2008), Depth dependency of the
110 Paleocene-Eocene carbon isotope excursion: Paired benthic and terrestrial biomarker records
111 (Ocean Drilling Program Leg 208, Walvis Ridge), *Geochem. Geophys. Geosyst.*, *9*(10), Q10008,
112 doi:10.1029/2008gc002116.
113 McInerney, F. A., and S. L. Wing (2011), The Paleocene-Eocene Thermal Maximum: A Perturbation of
114 Carbon Cycle, Climate, and Biosphere with Implications for the Future, *Annu. Rev. Earth Planet.*
115 *Sci.*, *39*(1), 489-516, doi:doi:10.1146/annurev-earth-040610-133431.
116 Nicolo, M. J., G. R. Dickens, C. J. Hollis, and J. C. Zachos (2007), Multiple early Eocene hyperthermals:
117 Their sedimentary expression on the New Zealand continental margin and in the deep sea,
118 *Geology*, *35*(8), 699-702, doi:10.1130/g23648a.1.
119 Nunes, F., and R. D. Norris (2006), Abrupt reversal in ocean overturning during the Palaeocene/Eocene
120 warm period, *Nature*, *439*(7072), 60-63.
121 Pagani, M., N. Pedentchouk, M. Huber, A. Sluijs, S. Schouten, H. Brinkhuis, J. S. Sinninghe Damste, G.
122 R. Dickens, and S. Expedition (2006), Arctic hydrology during global warming at the
123 Palaeocene/Eocene thermal maximum, *Nature*, *442*(7103), 671-675,
124 doi:http://www.nature.com/nature/journal/v442/n7103/suppinfo/nature05043_S1.html.
125 Pearson, P. N., P. W. Ditchfield, J. Singano, K. G. Harcourt-Brown, C. J. Nicholas, R. K. Olsson, N. J.
126 Shackleton, and M. Hall (2001), Warm tropical sea surface temperatures in the Late Cretaceous
127 and Eocene epochs, *Nature*, *413*, 481-487.
128 Pearson, P. N., and C. E. Burgess (2008), Foraminifer test preservation and diagenesis: comparison of
129 high latitude Eocene sites, in *Biogeochemical Controls on Palaeoceanographic Environmental*
130 *Proxies*, edited by W. E. N. Austin and R. H. James, pp. 59-72, Geological Society, London,
131 Special Publications.
132 Penman, D. E., B. Hönisch, R. E. Zeebe, E. Thomas, and J. C. Zachos (2014), Rapid and sustained
133 surface ocean acidification during the Paleocene-Eocene Thermal Maximum, *Paleoceanography*,
134 *29*(5), 2014PA002621, doi:10.1002/2014pa002621.
135 Penman, D. E., S. K. Turner, P. F. Sexton, R. D. Norris, A. J. Dickson, S. Boulila, A. Ridgwell, R. E.
136 Zeebe, J. C. Zachos, and A. Cameron (2016), An abyssal carbonate compensation depth
137 overshoot in the aftermath of the Palaeocene-Eocene Thermal Maximum, *Nature Geoscience*,
138 *9*(8), 575-580.
139 Ridgwell, A. (2007), Interpreting transient carbonate compensation depth changes by marine sediment
140 core modeling, *Paleoceanography*, *22*(4).
141 Sager, W. W., E. L. Winterer, and J. V. Firth (1993), Proceedings of the Ocean Drilling Program. Initial
142 Report 143.
143 Schrag, D. P., D. J. DePaolo, and F. M. Richter (1995), Reconstructing past sea surface temperatures:
144 Correcting for diagenesis of bulk marine carbonate, *Geochim. Cosmochim. Acta*, *59*, 2265-2278.
145 Schrag, D. P. (1999), Effects of diagenesis on the isotopic record of late paleogene tropical sea surface
146 temperatures, *Chem. Geol.*, *161*(1-3), 215-224, doi:10.1016/s0009-2541(99)00088-1.
147 Sexton, P. F., P. A. Wilson, and P. N. Pearson (2006), Microstructural and geochemical perspectives on
148 planktic foraminiferal preservation: "Glassy" versus "Frosty", *Geochemistry Geophysics*
149 *Geosystems*, *7*(12), doi:10.1029/2006GC001291.
150 Si, W., and M.-P. Aubry (2018), Vital Effects and Ecologic Adaptation of Photosymbiont-Bearing
151 Planktonic Foraminifera During the Paleocene-Eocene Thermal Maximum, Implications for
152 Paleoclimate, *Paleoceanography and Paleoclimatology*, *33*(1), 112-125,
153 doi:10.1002/2017PA003219.

154 Sluijs, A., H. Brinkhuis, S. Schouten, S. M. Bohaty, C. M. John, J. C. Zachos, G.-J. Reichart, J. S.
155 Sinninghe Damste, E. M. Crouch, and G. R. Dickens (2007), Environmental precursors to rapid
156 light carbon injection at the Palaeocene/Eocene boundary, *Nature*, *450*(7173), 1218-1221,
157 doi:http://www.nature.com/nature/journal/v450/n7173/suppinfo/nature06400_S1.html.
158 Spero, H. J., J. Bijma, D. W. Lea, and B. E. Bemis (1997), Effect of seawater carbonate concentration on
159 foraminiferal carbon and oxygen isotopes, *Nature*, *390*(6659), 497-500.
160 Storey, M., R. A. Duncan, and C. C. Swisher (2007), Paleocene-Eocene Thermal Maximum and the
161 Opening of the Northeast Atlantic, *Science*, *316*(5824), 587-589, doi:10.1126/science.1135274.
162 Svensen, H., S. Planke, A. Malthe-Sorenssen, B. Jamtveit, R. Myklebust, T. Rasmussen Eidem, and S. S.
163 Rey (2004), Release of methane from a volcanic basin as a mechanism for initial Eocene global
164 warming, *Nature*, *429*(6991), 542-545.
165 Thomas, E. (1990), Late Cretaceous-early Eocene mass extinctions in the deep sea., in *Global*
166 *Catastrophes in Earth History: An Interdisciplinary Conference on Impacts, Volcanism, and*
167 *Mass Mortality*, edited by V. L. Sharpton and P. D. Ward, pp. 481-495, Geological Society of
168 America Special Papers.
169 Thomas, E., and N. J. Shackleton (1996), *The Palaeocene-Eocene benthic foraminiferal extinction and*
170 *stable isotope anomalies.*, Geological Society London, Special Publication 4, 9, London.
171 Thomas, E. (2003), Benthic foraminiferal record across the Initial Eocene Thermal Maximum, Southern
172 Ocean Site 690, *Causes and consequences of globally warm climates in the Early Paleogene*,
173 *369*, 319.
174 Tripati, A. K., M. L. Delaney, J. C. Zachos, L. D. Anderson, D. C. Kelly, and H. Elderfield (2003),
175 Tropical sea-surface temperature reconstruction for the early Paleogene using Mg/Ca ratios of
176 planktonic foraminifera, *Paleoceanography*, *18*(4), 1101, doi:10.1029/2003pa000937.
177 Uchikawa, J., and R. E. Zeebe (2010), Examining possible effects of seawater pH decline on
178 foraminiferal stable isotopes during the Paleocene-Eocene Thermal Maximum,
179 *Paleoceanography*, *25*(2), PA2216, doi:10.1029/2009pa001864.
180 Valley, J. W., and N. T. Kita (2009), *In situ* oxygen isotope geochemistry by ion microprobe, in *MAC*
181 *Short Course: Secondary Ion Mass Spectrometry in the Earth Sciences*, edited by M. Fayek, pp.
182 16-63.
183 Westerhold, T., U. Röhl, T. Frederichs, C. Agnini, I. Raffi, J. C. Zachos, and R. H. Wilkens (2017),
184 Astronomical calibration of the Ypresian timescale: implications for seafloor spreading rates and
185 the chaotic behavior of the solar system?, *Climate of the Past*, *13*(9), 1129.
186 Wing, S. L., G. J. Harrington, F. A. Smith, J. I. Bloch, D. M. Boyer, and K. H. Freeman (2005), Transient
187 Floral Change and Rapid Global Warming at the Paleocene-Eocene Boundary, *Science*,
188 *310*(5750), 993-996, doi:10.1126/science.1116913.
189 Zachos, J. C., M. W. Wera, S. Bohaty, M. L. Delaney, M. R. Petrizzo, A. Brill, T. J. Bralower, and I.
190 Premoli-Silva (2003), A transient rise in tropical sea surface temperature during the Paleocene-
191 Eocene Thermal Maximum, *Science*, *302*, 1551-1554, doi:10.1126/science.1090110.
192 Zachos, J. C., et al. (2005), Rapid Acidification of the Ocean During the Paleocene-Eocene Thermal
193 Maximum, *Science*, *308*(5728), 1611-1615, doi:10.1126/science.1109004.
194 Zachos, J. C., S. M. Bohaty, C. M. John, H. McCarren, D. C. Kelly, and T. Nielsen (2007), The
195 Palaeocene–Eocene carbon isotope excursion: constraints from individual shell planktonic
196 foraminifer records, *Philosophical Transactions of the Royal Society A: Mathematical, Physical*
197 *and Engineering Sciences*, *365*(1856), 1829-1842, doi:10.1098/rsta.2007.2045.
198 Zeebe, R. E., J. C. Zachos, and G. R. Dickens (2009), Carbon dioxide forcing alone insufficient to explain
199 Palaeocene-Eocene Thermal Maximum warming, *Nature Geoscience*, *2*, 576-580,
200 doi:10.1038/NGEO578.
201 Zhang, Q., I. Wendler, X. Xu, H. Willems, and L. Ding (2017), Structure and magnitude of the carbon
202 isotope excursion during the Paleocene-Eocene thermal maximum, *Gondwana Research*, *46*, 114-
203 123.

204